ADVANCED FUNCTIONAL MATERIALS
www.afm-journal.de

# "1+2" Alloy-Like Strategy: Restricting Molecular Diffusion Enables Highly Thermally-Stable and Efficient Organic Solar Cells

*Jin Chen, Yao Wu, Liangliang Chen,* Yuchen Liao, Yanzhuo Zhu, Aziz Saparbaev, Ming Wan, Jingnan Wu, Yuda Li, Huimin Xiang, Adolat Saidkulova, Xunchang Wang,* and Renqiang Yang**

**Achieving concurrent enhancement in both power conversion efficiency (PCE) and long-term durability of organic solar cells (OSCs) is challenging for their commercial applications. Despite the critical roles of small molecule acceptors in achieving high photovoltaic performance, they suffer from inherent diffusion tendencies under operational conditions due to weak intermolecular interaction and small-sized structure, commonly leading to significant device degradation. Herein, a "1+2" alloy-like strategy consisting of monomer L8-BO and dimer D-Y3F in the ternary active blend is developed, which effectively realizes molecular diffusion restriction and morphology stabilization while achieving a remarkable PCE of 19.70%. The PM6:L8-BO:D-Y3F system demonstrates exceptional thermal stability, retaining over 85% of its initial PCE after 200 h of thermal aging at 85 °C. This alloy-like approach synergistically enhances device performance and stability through multiple mechanisms: 1) controlling pre-aggregation behavior and optimizing the nano-micromorphology to promote exciton dissociation and charge transport; 2) suppressing severe molecular diffusion by D-Y3F-induced robust network with enhanced $\pi$–$\pi$ interaction and molecular entanglement in the alloy-like composite; 3) regulating relatively higher glass transition temperature to overcome the diffusion-driven morphological evolution such as aggregation and phase separation. The work provides a promising approach for realizing high-performance OSCs while effectively mitigating diffusion-induced device degradation.**

## 1. Introduction

Bulk heterojunction (BHJ) organic solar cells (OSCs) have garnered considerable interest due to their desirable attributes, such as flexibility, lightweight nature, and customizable coloration.[1–8] Especially, the materials evolution of the high-performing small molecule acceptor (SMA) Y6 and its derivatives (Y-series SMAs) as well as device engineering have driven the power conversion efficiency (PCE) of single-junction OSCs exceeding 20%.[9–15] Despite these advancements, these state-of-art Y-series SMAs still face critical challenges, particularly the apparent molecular diffusion tendency during kinetic-to-thermodynamic equilibrium transitions owing to their relatively low glass transition temperature ($T_g$) and high diffusion coefficient within the donor.[16–18] Such diffusion behavior inevitably destabilizes the optimal morphology during long-term device operation, thus leading to reduced device stability. Therefore, developing an effective stabilization strategy to restrict molecular diffusion is a crucial

J. Chen, L. Chen, Y. Liao, M. Wan, H. Xiang, X. Wang, R. Yang
Key Laboratory of Flexible Optoelectronic Materials and Technology (Ministry of Education), School of Optoelectronic Materials & Technology
Jianghan University
Wuhan 430056, China
E-mail: chenliangliang@jhun.edu.cn; wangxc@jhun.edu.cn; yangrq@jhun.edu.cn

Y. Wu, Y. Zhu, Y. Li
Key Laboratory of Novel Biomass-based Environmental and Energy Materials in Petroleum and Chemical Industry, School of Chemical Engineering and Pharmacy
Wuhan Institute of Technology
Wuhan 430205, China

A. Saparbaev, A. Saidkulova
Institute of Ion-Plasma and Laser Technologies, Uzbekistan Academy of Sciences
National University of Uzbekistan
Tashkent 100125, Uzbekistan

J. Wu
Department of Chemistry and Chemical Engineering
Chalmers University of Technology
Göteborg 41296, Sweden

The ORCID identification number(s) for the author(s) of this article can be found under https://doi.org/10.1002/adfm.202508397

**DOI: 10.1002/adfm.202508397**

 

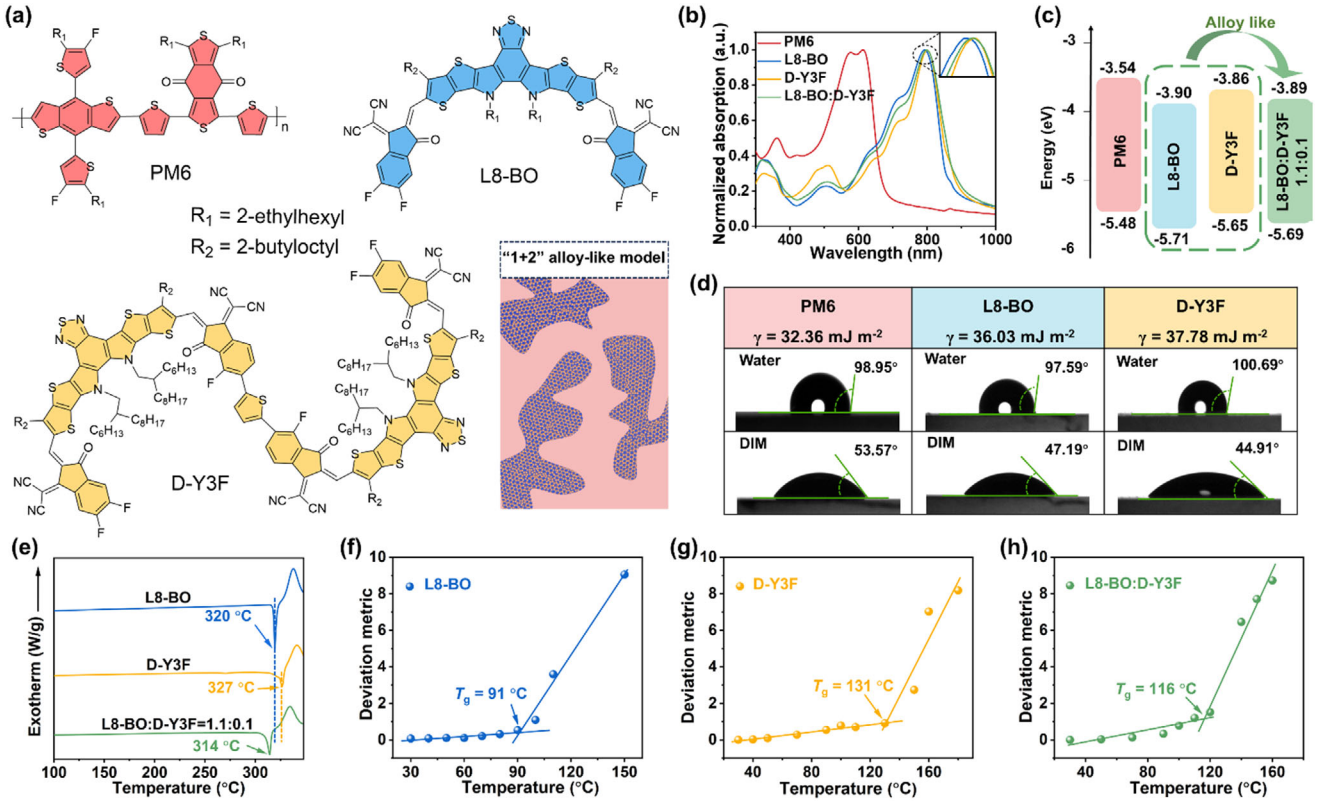


**Figure 1.** a) Chemical structures of PM6, L8-BO, and dimer D-Y3F, and schematic diagram of the microscopic morphology of "1+2" alloy-like model. b) Normalized UV–vis absorption of PM6, L8-BO, D-Y3F and L8-BO:D-Y3F (1.1:0.1) films. c) The energy level diagrams of relevant materials and the L8-BO:D-Y3F mixed materials. d) Contact angles of water and DIM on the films of PM6, L8-BO, and D-Y3F. e) DSC curves of L8-BO, D-Y3F neat acceptors and L8-BO:D-Y3F blend. The measurements of $T_g$ values by fitting UV–vis deviation metric results of f) L8-BO, g) D-Y3F, and h) L8-BO:D-Y3F (1.1:0.1) films.

requirement for realizing a balance between the stability and efficiency of OSCs.

Dimerized small-molecule acceptors (DSMAs) incorporate the advantages of both small molecules and polymers with definite chemical structures and low diffusion properties, offering a satisfactory PCE comparable to SMAs, as well as the mitigated tendency of molecular diffusion close to polymer acceptors.[19–27] For example, Kim et al. connected two Y-series monomers by vinylene unit to afford a dimeric acceptor DYV with a high $T_g$ of 134 °C, and the binary OSC device based on PM6:DYV demonstrates a high PCE of 18.60% and excellent stability with 80% of their initial efficiency ($T_{80}$) up to 4005 h under 1-sun illumination.[28] Wei et al. dimerized two Y-series monomers by a thiophene unit, achieving a higher PCE of 18.19%, and enhanced stability in comparison with its monomer.[29] Notably, DSMAs and SMAs are structurally similar, which might synergistically work together in the active layer by forming alloy-like composites due to high molecular compatibility and further enhance the PCE and stability of OSCs.[30–38] For example, Alex et al. developed an alloy-like acceptor *d*T9TBO:Y6 and the corresponding ternary device displays excellent thermal stability with negligible decay after 1800 h under 65 °C thermal stress.[31] These studies collectively highlight the significance of the alloy-like phase, formed of DSMA/SMA combination, in advancing the development of high-performance OSCs. Therefore, it is necessary to further explore the mechanism for the trade-off between efficiency and stability by DSMAs-based alloy-like strategy. Moreover, quantitative analysis of SMAs diffusion via comprehensive morphological parameter analysis in high-efficiency systems to elucidate the diffusion-thermal property relationship under long-term high-temperature conditions for enhanced device stability is crucial, which will take an important step toward enhancing OSCs efficiency and stability.

In this work, we designed a "1+2" alloy-like strategy consisting of L8-BO and its dimerized analog, D-Y3F (**Figure 1a**). With stronger intermolecular interaction, the L8-BO:D-Y3F alloy-like acceptor exhibits enhanced molecular packing behavior compared to pure L8-BO, forming a more robust integrated network. This structural reinforcement, coupled with increased molecular entanglement in the alloy-like composite, significantly elevates the kinetic energy barrier for molecular motion, and thereby effectively suppresses the molecular diffusion process. High-temperature morphology stability and thermal property measurement reveal that this L8-BO:D-Y3F alloy-like phase exhibits a significantly higher $T_g$ of 116 °C compared to L8-BO ($T_g$ = 91 °C) owing to incorporating of D-Y3F ($T_g$ = 131 °C), resulting in lower molecular diffusion coefficient of L8-BO:D-Y3F mixture, which contributes to robust microstructure in PM6:L8-BO:D-Y3F ternary system, thereby overcoming the morphological evolution of the active layer at high temperature and dramatically

improving thermal stability. The suppressed thermally-driven phase separation via this dimer alloy-like strategy endows the device with higher endurance under thermal stress, with a PCE maintenance of over 85% after heating at 85 °C for 200 h. Meanwhile, the "1+2" alloy-like strategy is also found to promote exciton dissociation and improve charge transport, resulting in an increased PCE of 19.70% for PM6:L8-BO:D-Y3F system. This work demonstrates that the "1+2" alloy-like strategy presented in this study provides valuable insights on simultaneously boosting efficiency and stability in ternary OSCs.

## 2. Results and Discussion

### 2.1. Synthesis and Characterization of Materials

The synthetic details and corresponding characterizations of dimer acceptor D-Y3F, including $^{1}H$ and $^{13}C$ NMR spectroscopy, and mass spectra analysis are presented in the Supporting Information (Scheme S1, and Figures S1–S5, Supporting Information). The UV–vis absorption spectrum is depicted in Figure 1b, which reveals that the absorption of D-Y3F and the blended acceptors are marginally red-shifted relative to L8-BO, which is attributed to the enhanced intermolecular interaction and elongated conjugated length of dimerized molecules. Moreover, D-Y3F exhibits a higher absorption coefficient of $1.65 \times 10^{6}$ $M^{-1}$ $cm^{-1}$ than that of L8-BO ($0.99 \times 10^{6}$ $M^{-1}$ $cm^{-1}$), demonstrating its stronger capability for light harvesting (Figure S6 and Table S1, Supporting Information). Fourier-transform infrared spectroscopy (FTIR) was used to evaluate the interactions between L8-BO and D-Y3F. As shown in Figure S7 (Supporting Information), the stretching vibrations of C═O and —$CH_2$— give rise to distinct absorption peaks at 1694.2 and 2856.3 $cm^{-1}$ for L8-BO, and 1693.8 and 2854.0 $cm^{-1}$ for L8-BO:D-Y3F, respectively. The L8-BO:D-Y3F mixture exhibits blue shifts in absorption peaks compared to the L8-BO, suggesting strong van der Waals interactions between L8-BO and D-Y3F.[14,39]

Considering the high similarity of the chemical structure of D-Y3F and L8-BO, these two acceptors might exhibit good compatibility to form an alloy-like phase in the blend film.[40] To validate the formation of alloy-like acceptor of D-Y3F and L8-BO mixture, cyclic voltammetry was carried out to detect the variation of energy levels with the different ratios of D-Y3F and L8-BO. It can be found that the LUMO energy levels of L8-BO:D-Y3F blends gradually increased with the increase of D-Y3F content, which is considered as a common feature of forming an alloy-like state (Figure 1c; Figures S8 and S9 and Table S2, Supporting Information).[41] Subsequently, contact angle tests were performed to explore the compatibility and miscibility among PM6, L8-BO, and D-Y3F. The surface energies ($\gamma$) of neat PM6, L8-BO and D-Y3F are determined to be 32.36, 36.03, 37.78 mJ $m^{-2}$, respectively (Figure 1d). Meanwhile, the calculated Flory–Huggins interaction parameters ($\chi$) follow the trend of L8-BO:D-Y3F (0.021 K) < PM6:L8-BO (0.098 K) < PM6:D-Y3F (0.210 K) (Table S3, Supporting Information). The similar surface energies between L8-BO and D-Y3F and their lower $\chi$ parameter versus PM6:L8-BO and PM6:D-Y3F blends indicate these two acceptors have superior miscibility and prefer to form the alloy-like phase in the ternary blend.[42]

To further verify the formation of the alloy-like state between L8-BO and D-Y3F, the melting transition points ($T_m$) of these acceptors were assessed by differential scanning calorimetry (DSC, Figure 1e), respectively. After blending L8-BO and D-Y3F, the blend exhibits only an endothermic peak with $T_m$ of ≈314 °C, which is between the corresponding two $T_m$s in pure materials (the $T_m$ of pure L8-BO and D-Y3F are ≈320 and ≈327 °C). The significantly reduced $T_m$ of the L8-BO:D-Y3F blend also provides convincing evidence for their exceptional miscibility to form the alloy-acceptor phase.[43]

To evaluate the potential of D-Y3F in optimizing the stability of PM6:L8-BO based binary OSCs device, we assessed the $T_g$ values for pure SMA and alloyed system by referring to the deviation metric method (Figure 1f–h).[44,45] After analyzing the thin film absorption spectra at various annealing temperatures, the $T_g$ values are determined to be 91 °C for L8-BO, 131 °C for D-Y3F, and 116 °C for L8-BO:D-Y3F blend, respectively. The higher $T_g$ of dimer D-Y3F compared to pure L8-BO is attributed to the strong intermolecular interaction induced by large dipole moment (DFT calculation in Figure S10, Supporting Information) and extended conjugation backbone.[46] Besides, according to the electrostatic potential (ESP) mapping, both L8-BO and D-Y3F exhibit negative potentials at their end-capping groups and relatively positive potentials at their central cores. It implies that similar to the self-packing of L8-BO, the possible interaction sites between L8-BO and D-Y3F are still end-to-end and core-to-core.[47,48] In addition, the high planarity of dimer and similar backbone structure between L8-BO and D-Y3F are feasible to obtain tight molecular packing behavior (discussed in GIWAXS section below) in alloy-like phase, limiting the molecular motion and immobilizing the morphology in the blend film. These characteristics enable D-Y3F to act as a multifunctional component that simultaneously facilitates alloy-like phase formation and stabilizes blend morphology by suppressing L8-BO diffusion, thus contributing to enhanced device stability.

### 2.2. Photovoltaic Properties and Working Mechanism

To investigate the photovoltaic performance based on L8-BO:D-Y3F alloy-like acceptor, a conventional device structure of ITO/2PACz/Active layer/PDINN/Ag was applied to fabricate OSCs. The *J*–*V* characteristics of optimized binary and ternary devices were measured under an AM 1.5G solar simulator, as depicted in **Figures 2a** and S11 (Supporting Information), with the relevant photovoltaic parameters summarized in **Table 1** and Table S4 (Supporting Information). The controlled binary device based on PM6:L8-BO exhibits an optimized PCE of 18.40% with an open-circuit voltage ($V_{oc}$) of 0.876 V, a short-circuit current ($J_{sc}$) of 26.69 mA $cm^{-2}$, and a fill factor (FF) of 78.7%. Attributed to narrower LUMO offset, the binary device based on PM6:D-Y3F obtains the high $V_{oc}$ of 0.926 V, yet with a low PCE of 15.41%, which may be attributed to the unfavorable morphology of the corresponding film (discussed below). In contrast, the optimized ternary PM6:L8-BO:D-Y3F device in a weight ratio of 1:1.1:0.1 (w/w) demonstrates synchronized enhancement in all photovoltaic parameters, boosting the PCE to 19.70%, ranking one of the highest values for DMSA based ternary system.[24,43,44,49–56] The external quantum efficiency (EQE) curves of the optimized

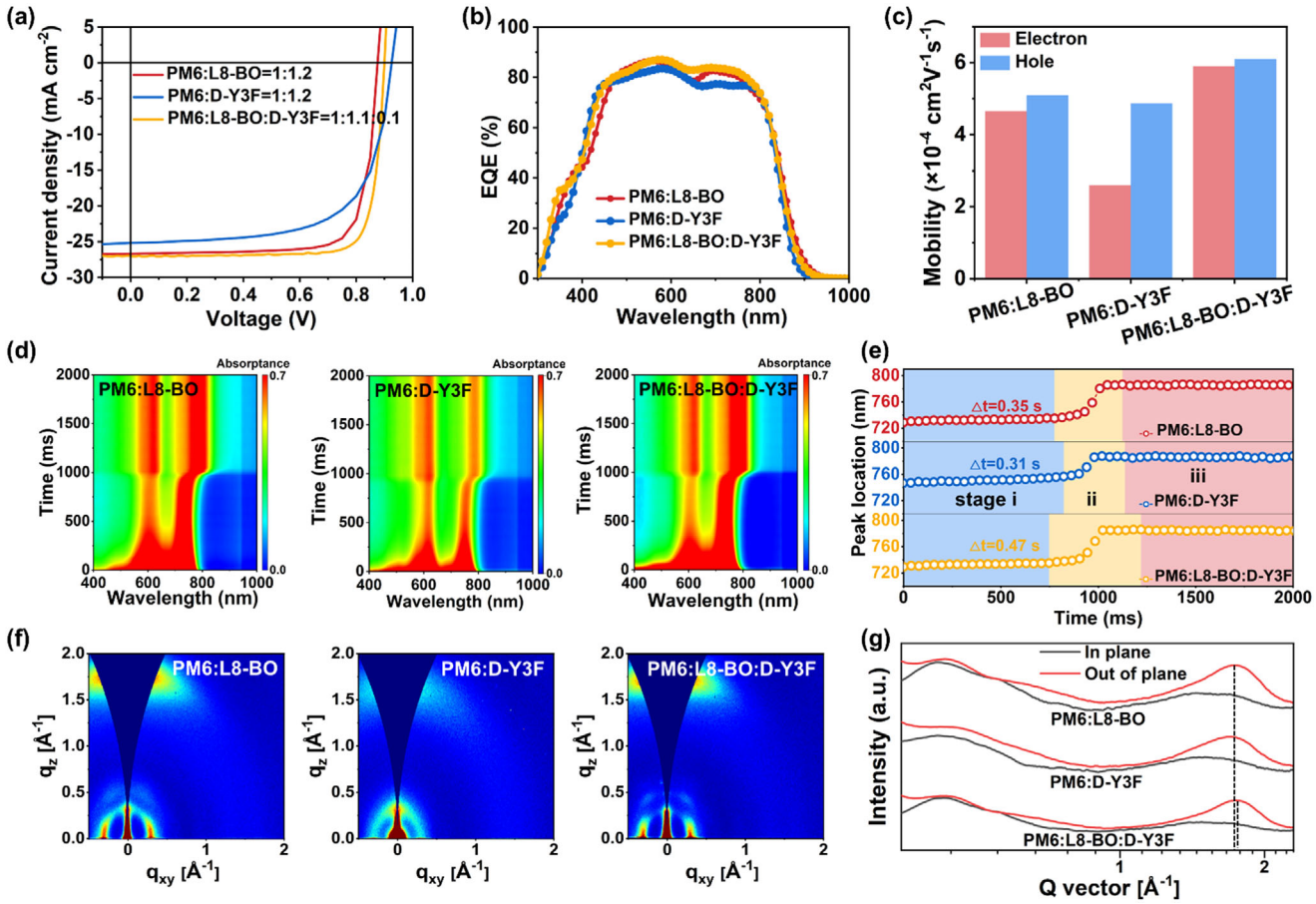


**Figure 2.** a) *J–V* characteristics for the binary and ternary devices. b) EQE curves of the corresponding OSCs. c) Electron and hole mobilities of the devices obtained from SCLC measurements. d) Time-dependent contour maps of in situ UV–vis absorption spectra of the three BHJs. e) Time evolution of the acceptor peak locations of the three BHJs. f) 2D GIWAXS images of the three BHJs. g) IP and OOP extracted line-cut profiles of the three BHJs.

devices are displayed in Figure 2b. The integrated $J_{sc}$ values of these devices from the EQE curves match well with those obtained from *J–V* test (<5% deviation). Interestingly, the onset of photo-response in PM6:L8-BO:D-Y3F shows sharper edges than that of PM6:L8-BO devices, suggesting lower radiative loss in ternary devices.[57]

To understand the remarkable enhancement in PCE achieved by the "1+2" alloy-like strategy, the charge transport ability was evaluated by space-charged limited current (SCLC) methods as shown in Figure 2c, Figure S12 and Table S5 (Supporting Information), from which the optimized hole mobilities ($\mu_h$) and electron mobilities ($\mu_e$) of blend films were assessed. The ternary device ($\mu_h = 6.10 \times 10^{-4}$ cm$^2$ V$^{-1}$ s$^{-1}$, $\mu_e = 5.90 \times 10^{-4}$ cm$^2$ V$^{-1}$ s$^{-1}$, $\mu_h/\mu_e = 1.03$) shows more balanced and higher charge mobilities than those of PM6:L8-BO ($\mu_h = 5.10 \times 10^{-4}$ cm$^2$ V$^{-1}$ s$^{-1}$, $\mu_e = 4.68 \times 10^{-4}$ cm$^2$ V$^{-1}$ s$^{-1}$, $\mu_h/\mu_e = 1.09$), and PM6:D-Y3F ($\mu_h = 4.87 \times 10^{-4}$ cm$^2$ V$^{-1}$ s$^{-1}$, $\mu_e = 2.60 \times 10^{-4}$ cm$^2$ V$^{-1}$ s$^{-1}$, $\mu_h/\mu_e = 1.87$) device, which constrict bimolecular recombination in the alloy-like system. The efficiencies of exciton dissociation and charge collection were investigated via the dependence of the photocurrent density ($J_{ph}$) on the effective internal voltage ($V_{eff}$) (Figure S13, Supporting Information). Generally, the current density of all devices saturates at low voltage (<0.5 V), indicating low trap-assisted recombination. The PM6:L8-BO device and PM6:L8-BO:D-Y3F device have higher saturated photocurrent densities, which is consistent with the EQE spectra. In

**Table 1.** Photovoltaic parameters of the binary and ternary OSCs under the illumination of AM 1.5G at 100 mW cm$^{-2}$.

| Active Layer | $V_{oc}$ [V] | $J_{sc}$ [mA cm$^{-2}$] | $J_{sc,cal}$ [a)] [mA cm$^{-2}$] | FF [%] | PCE [%] |
|---|---|---|---|---|---|
| PM6:L8-BO | 0.876 | 26.69 | 25.89 | 78.7 | 18.40 (18.13 ± 0.27) |
| PM6:D-Y3F | 0.926 | 25.18 | 24.57 | 66.1 | 15.41 (15.01 ± 0.40) |
| PM6:L8-BO:D-Y3F | 0.903 | 26.98 | 26.10 | 80.9 | 19.70 (19.39 ± 0.31) |

[a)] The $J_{sc,cal}$ represents the integrated current density obtained from EQE spectra.

addition, the alloy-like system improves the exciton dissociation efficiency up to 99.2% in comparison with PM6:L8-BO (97.5%), and PM6:D-Y3F (95.4%) system. The charge collection efficiency is also slightly upshifted, which is 84.5% for PM6:L8-BO, 79.5% for PM6:D-Y3F, and 85.7% for PM6:L8-BO:D-Y3F devices, respectively. Notably, the alloy-like system has more efficient exciton dissociation and charge collection, resulting in higher $J_{sc}$.

Moreover, the dependences of $V_{oc}$ and $J_{sc}$ on $P_{light}$ were measured to further elucidate the charge recombination mechanism (Figure S14, Supporting Information). Compared with the dimer-based binary device, the ternary device exhibited a smaller $V_{oc}$ dependence on light intensity with a slope of 1.02 $kT/q$ than that of PM6:L8-BO device (1.06 $kT/q$), indicating that trap-assisted recombination losses in the ternary device have been suppressed.[58] Then we analyzed the total trap density ($N_t$) by the SCLC method as shown in Figure S15 (Supporting Information). The ternary device has the lowest $N_t$ value of $3.37 \times 10^{16}$ cm$^{-3}$, while the PM6:L8-BO device has a relatively high $N_t$ value of $4.99 \times 10^{16}$ cm$^{-3}$, which further demonstrates lower trap-assisted recombination losses in ternary device.

To further explore how the "1+2" alloy-like strategy affects the pre-aggregation behaviors during the film formation process, the in situ UV–vis absorption was conducted as shown in Figure 2d and Figure S16 (Supporting Information). The process of film formation could be divided into three stages: i) solvent evaporation with invariant acceptor absorption peaks, ii) nucleation/crystallization marked by rapid red-shifting peaks due to molecular aggregation and enhanced intermolecular interactions, and iii) stabilized film formation with constant peak positions.[56] The crystallization time is defined by the duration of stage ii, as determined by in situ UV–vis spectral evolution. According to the time evolution of the acceptor peak locations, the crystallization times of the films based on PM6:L8-BO, PM6:D-Y3F, and PM6:L8-BO:D-Y3F are estimated to be 0.35, 0.31, and 0.47 s, respectively (Figure 2e). The prolonged aggregation time of the ternary blend might be attributed to the slow co-crystallization kinetics of the alloy-like acceptor, which promotes thermodynamically favorable molecular packing with reduced energetic disorder.[59] The pre-aggregation behavior could further confirm the role of D-Y3F as an effective morphology stabilizer that suppresses L8-BO diffusion.

Grazing-incidence wide-angle X-ray scattering (GIWAXS) characterization was conducted to further explore the packing behaviors in pristine and blend films, as shown in Figure 2f,g and Figure S17 (Supporting Information), and corresponding parameters were summarized in Table S6. 2D GIWAXS patterns reveal that the (010) peaks of D-Y3F, L8-BO, and alloy-like acceptor are pronounced in the out-of-plane (OOP) direction, corresponding to $\pi$–$\pi$ stacking in the face-on direction (Figure S17, Supporting Information). The profiles of their (010) peaks exhibit almost no difference, resulting in a similar crystal coherence length (CCL) ≈17 Å, indicating these acceptors show high crystallinity. The $q_z$ values of (010) peaks of L8-BO, D-Y3F, and the alloy-like acceptor are estimated to be 1.722, 1.663, and 1.747 Å$^{-1}$, corresponding to the $\pi$–$\pi$ packing distances ($d_{\pi\text{-}\pi}$) of 3.65, 3.78, and 3.60 Å, respectively. These results indicate that the L8-BO:D-Y3F alloy-like phase exhibits enhanced molecular packing behavior through stronger $\pi$-$\pi$ interactions compared to pure L8-BO, which forms a more tightly integrated network and has great potential for restricting the L8-BO from diffusion in solid state. In the blend films, the (010) peak in OOP direction of the ternary blend exhibits a slightly larger $q_z$ value corresponding to a closer $\pi$–$\pi$ stacking distance ($d_{\pi\text{-}\pi}$ = 3.59 Å) and a shaper profile with larger CCL of 18.23 Å compared to the those of PM6:D-Y3F ($d_{\pi-\pi}$ = 3.73 Å, CCL = 15.03 Å) and PM6:L8-BO ($d_{\pi-\pi}$ = 3.64 Å, CCL = 17.55 Å). This indicates that the dimer structure, D-Y3F, has a promoting effect on the tighter molecular packing of the host acceptor L8-BO, which subtly optimizes the morphology of the ternary blend and contributes to excellent device performance.

### 2.3. Device Stability and Molecular Diffusion Thermally Dynamic

Considering that OSCs release a lot of heat during long-term operation, the excellent thermal stability of OSCs is also a prerequisite for their commercialization. As depicted in **Figure 3a**, the thermal stability of the binary and ternary devices was evaluated under thermal annealing at 85 °C. The PM6:L8-BO and PM6:D-Y3F binary devices suffered from a dramatic drop to 68.5% and 82.3% of its initial PCE value after thermal aging for 200 h, while the "1+2" alloy-like ternary device demonstrated significantly enhanced stability under the same conditions, retaining 86.8% of its initial efficiency after 200 h of continuous thermal aging. Photovoltaic parameters analysis revealed that the efficiency degradation predominantly originated from diminished FF values (Figure S18, Supporting Information). The obvious discrepancy of stability confirms that the dimer small molecule D-Y3F with higher $T_g$, when incorporated into the PM6:L8-BO system, can effectively mitigate the intrinsic thermodynamic instability under thermal stress.

To further demonstrate the reason and mechanisms of "1+2" alloy-like strategy in suppressing heat-induced morphological degradation, some detailed comparisons and analysis of morphological behaviors of thin films under thermal stress were conducted through atomic force microscopy (AFM), transmission electron microscopy (TEM) and GIWAXS measurements. AFM and TEM images reveal that all the binary and alloy-like ternary blends stored at ambient temperature possessed homogeneous morphology without obvious aggregation (Figure 3b–e). After applying thermal stress (150 °C for 200 h) to the corresponding films, it is evident of the AFM images that PM6:L8-BO film shows plenty of coarse fiber particles with significant molecular aggregation and large roughness (Figure 3f). Such aggregation behavior is dramatically suppressed in PM6:L8-BO:D-Y3F blend treated under the same condition (Figure 3h). The root-mean-square roughness ($R_q$) value of PM6:L8-BO increases from 1.24 to 8.56 nm (Figure 3b,c). Correspondingly, the TEM images also reveal a broader distribution of domain sizes accompanied by distinct cloud-like aggregate structures (Figure 3d,e). In stark contrast, the PM6:L8-BO:D-Y3F blend exhibits dramatically distinct morphological evolution from PM6:L8-BO. After thermal annealing, the alloy-like ternary system exhibits increased surface roughness from 1.19 to 1.90 nm, accompanied by moderate domain coarsening (Figure 3h). The TEM image also reveals well-maintained nanomorphology with minor cloud-like aggregates, and a uniform D/A mixing appeared. Therefore, both AFM and TEM characterizations demonstrate that incorporating D-Y3F to PM6:L8-BO system can effectively suppress the migration and

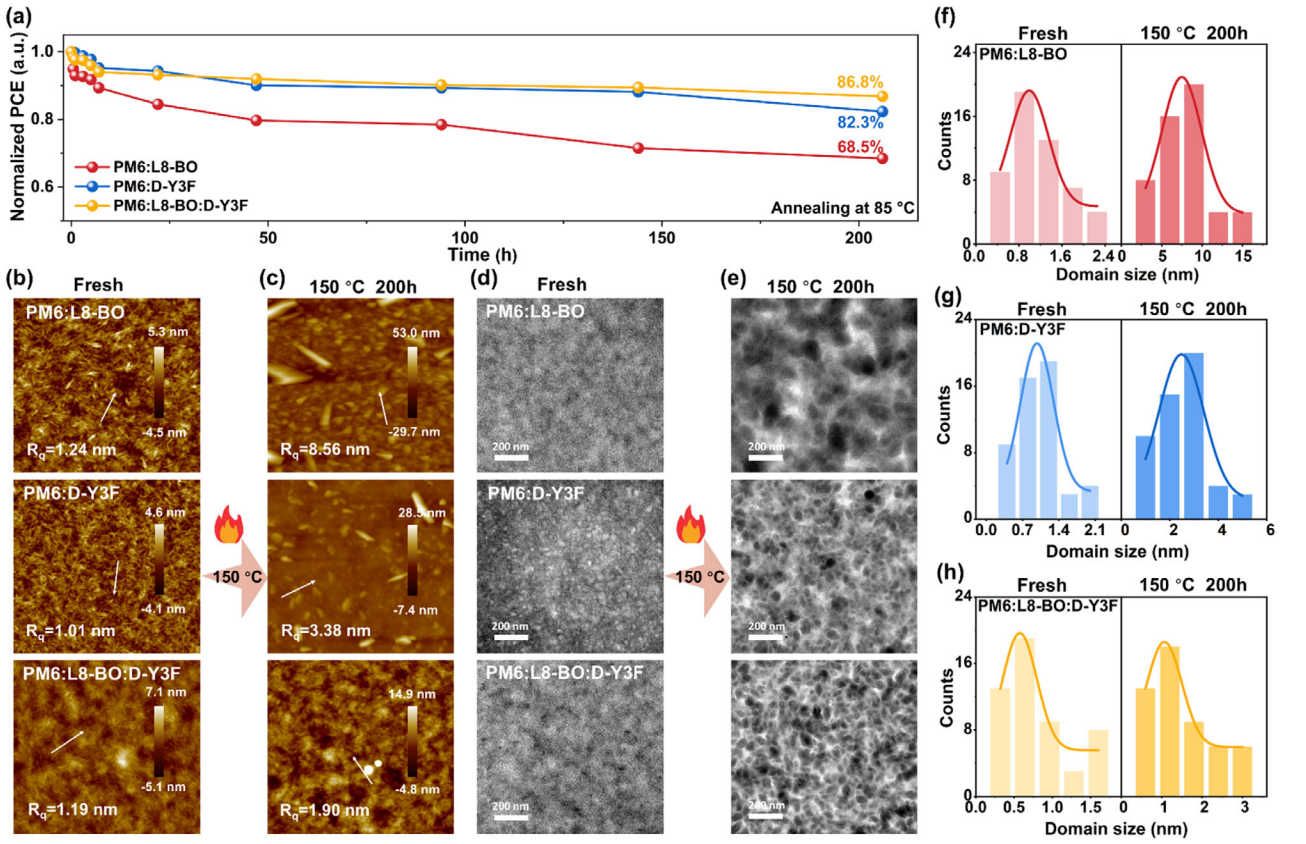


**Figure 3.** a) Normalized PCE of the corresponding OSCs after annealing at 85 °C. AFM images of the b) fresh and c) aged corresponding blend films (after annealing at 150 °C for 200 h, 2 μm × 2 μm). TEM images of the d) fresh and e) aged corresponding blend films (after annealing at 150 °C for 200 h). f–h) The distribution histogram of domain size along the arrow direction in AFM images of the corresponding fresh and aged blend films.

aggregation of L8-BO molecules and maintain the original blend morphology to a certain extent.

Additionally, we conducted the GIWAXS measurements with the fresh and thermal-aged active layers to investigate their variation of crystallization and intermolecular packing behavior. The diffraction patterns of the related blends are depicted in **Figure** 4a,b and corresponding 1D line-cut profiles are shown in Figure S19 (Supporting Information), with the corresponding fitting parameters summarized in Table S7 (Supporting Information). It should be noted that the significantly sharper (010) crystalline peak is observed in the PM6:L8-BO blend after 150 °C thermal annealing treatments for 200 h, demonstrating reduced half-widths and extended coherence lengths compared to the PM6:L8-BO:D-3YF blend. To quantify crystallinity evolution during aging, we define a normalized coherence length change parameter: $K_{CCL} = (CCL_{aged} - CCL_{fresh})/CCL_{fresh}$.[60] As shown in Figure 4c, the $K_{CCL}$ values in the OOP direction demonstrate distinct aging behaviors: PM6:L8-BO (32.8%) > PM6:D-Y3F (8.1%) > PM6:L8-BO:D-Y3F (5.4%). The quantitative analysis reveals markedly different thermal-aging-induced crystallization dynamics: PM6:L8-BO blend undergoes substantial crystallinity reorganization, while the PM6:L8-BO:D-Y3F system maintains optimal molecular packing after thermal aging. In addition, PM6:L8-BO:D-Y3F blend exhibits reduced (100) lamellar stacking intensity after thermal aging, in contrast to the behavior observed in PM6:L8-BO. This variation trend likely originates from enhanced side-chain entanglement within the thermally stabilized acceptor alloy-like phase, which effectively suppresses small-molecule diffusion, and thus does not experience significant performance attenuation under prolonged thermal stress. Thus, the above results further demonstrate that the strategy effectively stabilizes the nanoscale morphology in the solid state by suppressing diffusion-induced degradation, thereby simultaneously enhancing both device stability and photovoltaic performance.

To verify the dimer-induced entanglement effect in ternary blends, we conducted pseudo-free-standing tensile testing on the water surface, enabling direct measurement of mechanical properties through stress-strain (S-S) curves. Figure 4d displayed the S-S curves of binary and ternary films, with quantitative crack-onset strain (COS) analysis provided in Figure S20 (Supporting Information). It can be noted that the alloy-like ternary film demonstrates superior mechanical properties with 3.61% elongation, representing a 36% increase over the binary PM6:L8-BO. This enhanced ductility confirms improved film-forming characteristics through strengthened intermolecular chain entanglement in the alloy-phase system.[32]

Based on the comprehensive data obtained from the aforementioned tests, we propose a mechanistic model (Figure 4e,f) illustrating how the "1+2" alloy-like strategy governs BHJ morphological evolution. In the initial active layer, the binary and

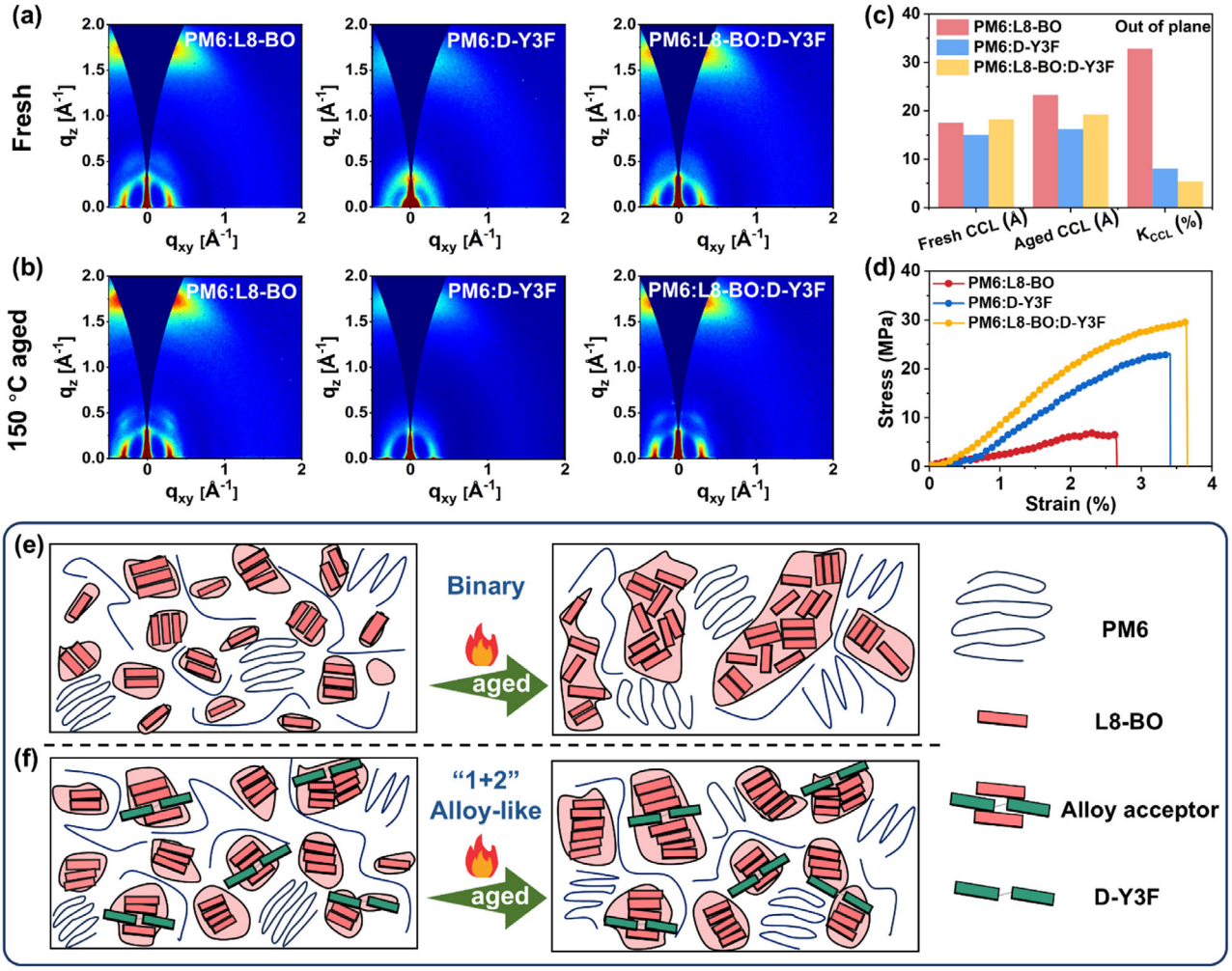


**Figure 4.** 2D GIWAXS patterns of a) fresh and b) aged corresponding blend films. c) Histograms of CCL and $K_{CCL}$ of the fresh and aged corresponding blend films. d) Representative stress-strain curves of the corresponding blend films. Schematic diagram of the changes in active layer morphology before and after thermal stress for e) PM6:L8-BO system and f) PM6:L8-BO:D-Y3F system.

alloy-like ternary systems exhibit appropriate phase separation and interconnected networks, enabling efficient exciton dissociation and charge transport. However, under thermal stress, the donor/acceptor phases in the binary system inevitably migrate toward thermodynamic equilibrium due to the lower $T_g$ of L8-BO, resulting in excessive molecular aggregation, severe phase separation (Figure 3b–e and 4e), and consequently degraded photovoltaic performance. In contrast, for ternary blends, the excellent miscibility between the host (L8-BO) and guest acceptors (D-Y3F) in the alloy-model acceptor leads to the formation of a tight and uniform phase between them, which achieves a fixed morphology due to the intermolecular interactions or chain entanglements in the "1+2" alloy-like system. The large dimer molecules with high $T_g$ not only act as an adhesive to elevate the kinetic energy barrier of molecular motion, mitigating the molecular diffusion process, but also optimize the pre-aggregation and molecular packing behavior to promote exciton dissociation and improve charge transport, resulting in a synergistic improvement of device efficiency and thermal stability.

To illustrate the advantages from the commercial or scalability standpoint of our "1+2" alloy-like strategy, we calculate the figure-of-merit (FOM) value, which has been widely used to quantitatively assess the cost-performance of photovoltaic materials used in possible OSC applications.[61,62] Compared with those of the representative high-performing binary system (PM6:Y6, PM6:L8-BO and PM6:BTP-eC9), a high FOM value of 0.265 was achieved based on PM6:L8-BO:D-Y3F system, which was mainly attributed to the fact that we have achieved the improvement of PCE by using a very small amount (PM6:L8-BO:D-Y3F = 1:1.1:0.1, w/w), thus having a very small impact on the cost but greatly improving PCE (Figure S21 and Tables S8 and S9 (Supporting Information). The lower FOM value demonstrates that D-Y3F has a good industrial application prospect in improving efficiency and stability.

## 3. Conclusion

In summary, we reported a "1+2" alloy-like strategy by introducing dimer D-Y3F as a functionalized third component into the PM6:L8-BO system to effectively enhance both the efficiency

and stability of OSCs. In terms of efficiency, the incorporation of D-Y3F not only precisely controls pre-aggregation behavior during the film-formation process, but also optimizes the nano-micromorphology to promote exciton dissociation and charge transport, resulting in an improved PCE of 19.70% in PM6:L8-BO:D-Y3F based OSCs. Regarding stability, we resolve the severe molecular diffusion issue of PM6:L8-BO system by D-Y3F-induced robust integrated network with enhanced $\pi$–$\pi$ interactions and molecular entanglement in the alloy-like composite. Moreover, the elevated $T_g$ of 116 °C of the alloy-like phase, compared to L8-BO ($T_g$ = 91 °C), facilitates the formation of a thermally robust microstructure in the alloy-like ternary system, effectively overcoming the morphological evolution of the active layer and dramatically improving thermal stability. Consequently, the PM6:L8-BO:D-Y3F system exhibited superior stability, retaining over 86.8% of its initial efficiency after continuous 85 °C aging for 200 h, while the PCE of the PM6:L8-BO declined to 68.5% under the same condition. We believe the "1+2" alloy-like strategy developed in this work establishes a new design paradigm for molecular diffusion restriction and morphology fixation, achieving concurrent enhancement in both power conversion efficiency and operational stability–a critical step toward practical photovoltaic applications.

## Supporting Information

Supporting Information is available from the Wiley Online Library or from the author.

## Acknowledgements

J.C. and Y.W. contributed equally to this work. The authors were deeply grateful to the National Natural Science Foundation of China (52203225, 22375077, 52073122, 22008184), Excellent Young and Middle-aged Science and Technology Innovation Team Program for Universities in Hubei Province (T2023037), Department of Science and Technology of Hubei Province (2024DJC006), Key R&D Project of Hubei Province (2022BAA095), Natural Science Foundation of Hubei Province (2022CFB903), Key Research and Development Program of Wuhan (2024010802030156), Ministry of Science and Technology of China (2021YFE0113600), China Postdoctoral Science (2023M742717), the Special Project from Jianghan University (2022XKZX02), and Excellent Discipline Cultivation Project by JHUN (2023XKZ010, 2023XKZ014), the Knowledge Innovation Program of Wuhan-Shuguang Project (2023020201020438).

## Conflict of Interest

The authors declare no conflict of interest.

## Data Availability Statement

The data that support the findings of this study are available in the supplementary material of this article.

## Keywords

alloy-like acceptor, organic solar cell, power conversion efficiency, thermal stability

Received: April 2, 2025
Revised: May 18, 2025
Published online:

[1] T. Ameri, *Nat. Energy* **2021**, *6*, 1007.
[2] S. Chen, S. Zhu, L. Hong, W. Deng, Y. Zhang, Y. Fu, Z. Zhong, M. Dong, C. Liu, X. Lu, K. Zhang, F. Huang, *Angew. Chem., Int. Ed.* **2024**, *63*, 202318756.
[3] H. Lu, W. Liu, G. Ran, Z. Liang, H. Li, N. Wei, H. Wu, Z. Ma, Y. Liu, W. Zhang, X. Xu, Z. Bo, *Angew. Chem., Int. Ed.* **2023**, *62*, 202314420.
[4] S. Jung, U. J. Yang, J. Oh, S. Jeong, Y. Cho, G. H. Lee, M. K. Choi, C. Yang, *Adv. Funct. Mater.* **2024**, *34*, 2406200.
[5] Y. Li, S. Song, S. Y. Park, J. Y. Kim, H. Y. Woo, *Sci. China Chem.* **2017**, *60*, 528.
[6] M. H. Jee, H. S. Ryu, D. Lee, W. Lee, H. Y. Woo, *Adv. Sci.* **2022**, *9*, 2201876.
[7] Z. Ge, J. Qiao, Y. Li, J. Song, X. Duan, Z. Fu, H. Hu, R. Yang, H. Yin, X. Hao, Y. Sun, *Angew. Chem., Int. Ed.* **2025**, *64*, 202413309.
[8] Z. Sun, H. Ma, S. Yang, Y. Cho, S. Lee, J. Park, T. L. H. Mai, W. Kim, S. Jeong, S. Kim, C. Yang, *Adv. Funct. Mater.* **2024**, *34*, 2403093.
[9] Y. Jiang, S. Sun, R. Xu, F. Liu, X. Miao, G. Ran, K. Liu, Y. Yi, W. Zhang, X. Zhu, *Nat. Energy* **2024**, *9*, 975.
[10] H. Chen, Y. Huang, R. Zhang, H. Mou, J. Ding, J. Zhou, Z. Wang, H. Li, W. Chen, J. Zhu, Q. Cheng, H. Gu, X. Wu, T. Zhang, Y. Wang, H. Zhu, Z. Xie, F. Gao, Y. Li, Y. Li, *Nat. Mater.* **2025**, *24*, 444.
[11] Z. Chen, J. Ge, W. Song, X. Tong, H. Liu, X. Yu, J. Li, J. Shi, L. Xie, C. Han, Q. Liu, Z. Ge, *Adv. Mater.* **2024**, *36*, 2406690.
[12] X. Zhang, H. Gao, Y. Kan, X. Wang, W. Zhang, K. Zhou, H. Xu, L. Ye, R. Yang, Y. Yang, X. Hao, Y. Sun, K. Gao, *Angew. Chem., Int. Ed.* **2025**, *64*, 202415583.
[13] H. Lu, W. Liu, G. Ran, J. Li, D. Li, Y. Liu, X. Xu, W. Zhang, Z. Bo, *Adv. Mater.* **2024**, *36*, 2307292.
[14] W. Miao, Y. Liu, Y. Wu, J. Liang, J. Xiong, T. Hu, Y. He, L. Chen, J. Shan, X. Wang, R. Yang, *Adv. Funct. Mater.* **2025**, *35*, 2501143.
[15] L. Wang, C. Chen, Z. Gan, J. Cheng, Y. Sun, J. Zhou, W. Xia, D. Liu, W. Li, T. Wang, *Adv. Mater.* **2025**, *37*, 2419923.
[16] J.-W. Lee, J. S. Park, H. Jeon, S. Lee, D. Jeong, C. Lee, Y.-H. Kim, B. J. Kim, *Chem. Soc. Rev.* **2024**, *53*, 4674.
[17] Q. Burlingame, X. Huang, X. Liu, C. Jeong, C. Coburn, S. R. Forrest, *Nature* **2019**, *573*, 394.
[18] K. An, W. Zhong, F. Peng, W. Deng, Y. Shang, H. Quan, H. Qiu, C. Wang, F. Liu, H. Wu, N. Li, F. Huang, L. Ying, *Nat. Commun.* **2023**, *14*, 2688.
[19] C. Sun, J.-W. Lee, C. Lee, D. Lee, S. Cho, S.-K. Kwon, B. J. Kim, Y.-H. Kim, *Joule* **2023**, *7*, 416.
[20] X. Yang, Y. Gao, L.-Y. Xu, X. Wu, X. Chen, Y. Shao, B. Xiao, S. Liu, J. Xia, R. Sun, J. Min, *Energy Environ. Sci.* **2024**, *17*, 5962.
[21] H. Zhuo, X. Li, J. Zhang, S. Qin, J. Guo, R. Zhou, X. Jiang, X. Wu, Z. Chen, J. Li, L. Meng, Y. Li, *Angew. Chem., Int. Ed.* **2023**, *62*, 202303551.
[22] F. Yi, M. Xiao, Y. Meng, H. Bai, W. Su, W. Gao, Z. Yao, G. Qi, Z. Liang, C. Jin, L. Tang, R. Zhang, L. Yan, Y. Liu, W. Zhu, W. Ma, Q. Fan, *Angew. Chem., Int. Ed.* **2024**, *63*, 202319295.
[23] Y. Liang, D. Zhang, Z. Wu, T. Jia, L. Lüer, H. Tang, L. Hong, J. Zhang, K. Zhang, C. J. Brabec, N. Li, F. Huang, *Nat. Energy* **2022**, *7*, 1180.
[24] M. Peng, H. Wu, L. Wu, J. Chen, R. Ma, Q. Fan, H. Tan, W. Zhu, H. Li, J. Ding, *J. Energy Chem.* **2024**, *95*, 263.
[25] M. Ghasemi, H. Hu, Z. Peng, J. J. Rech, I. Angunawela, J. H. Carpenter, S. J. Stuard, A. Wadsworth, I. McCulloch, W. You, H. Ade, *Joule* **2019**, *3*, 1328.
[26] Y. Ding, W. A. Memon, S. Xiong, S. Gong, M. Li, Z. Deng, H. Liu, Y. Liu, X. Chen, N. Zheng, F. He, *Adv. Mater.* **2025**, *37*, 2501671.

 

[27] C.-Y. Lin, B.-H. Jiang, P.-J. Weng, Y. Hsuan Lin, Y.-W. Su, H.-S. Shih, Z.-E. Shi, Y.-R. Lin, J. Vailassery, S.-S. Sun, C.-P. Chen, Y. J. Chang, *Chem. Eng. J.* **2024**, *494*, 153183.
[28] J.-W. Lee, C. Sun, C. Lee, Z. Tan, T. N.-L. Phan, H. Jeon, D. Jeong, S.-K. Kwon, Y.-H. Kim, B. J. Kim, *ACS Energy Lett.* **2023**, *8*, 1344.
[29] L. Zhang, Z. Zhang, D. Deng, H. Zhou, J. Zhang, Z. Wei, *Adv. Sci.* **2022**, *9*, 2202513.
[30] F. Liu, L. Zhou, W. Liu, Z. Zhou, Q. Yue, W. Zheng, R. Sun, W. Liu, S. Xu, H. Fan, L. Feng, Y. Yi, W. Zhang, X. Zhu, *Adv. Mater.* **2021**, *33*, 2100830.
[31] F. Qi, Y. Li, R. Zhang, F. R. Lin, K. Liu, Q. Fan, A. K.-Y. Jen, *Angew. Chem., Int. Ed.* **2023**, *135*, 202303066.
[32] C. Han, H. Gao, Y. Kan, X. Zhang, X. Jiang, C. Shen, L. Ni, Z. Lv, Z. Zhang, L. Wang, J. A. Zapien, Y. Yang, Y. Sun, K. Gao, *Adv. Energy Mater.* **2024**, *14*, 2304063.
[33] J. Wan, T. Wang, R. Sun, X. Wu, S. Wang, M. Zhang, J. Min, *Adv. Mater.* **2023**, *35*, 2302592.
[34] Q. An, J. Wang, W. Gao, X. Ma, Z. Hu, J. Gao, C. Xu, M. Hao, X. Zhang, C. Yang, F. Zhang, *Sci. Bull.* **2020**, *65*, 538.
[35] C. Zhang, M. Zhang, Q. Zhou, S. Chen, S. Kim, J. Yao, Z. Zhang, Y. Bai, Q. Chen, B. Chang, H. Fu, L. Xue, H. Wang, C. Yang, Z.-G. Zhang, *Adv. Funct. Mater.* **2023**, *33*, 2214392.
[36] A. D. de Zerio, C. Müller, *Adv. Energy Mater.* **2018**, *8*, 1702741.
[37] K.-N. Zhang, J.-J. Guo, L.-J. Zhang, C.-C. Qin, H. Yin, X.-Y. Gao, X.-T. Hao, *Adv. Funct. Mater.* **2021**, *31*, 2100316.
[38] H. Han Chiu, B.-H. Jiang, H. Chi Wang, X.-M. Su, Y.-H. Kang, Y.-W. Su, H.-S. Shih, C.-P. Chen, Y. J. Chang, *Chem. Eng. J.* **2023**, *469*, 143938.
[39] H. Chen, R. Zhang, X. Chen, G. Zeng, L. Kobera, S. Abbrent, B. Zhang, W. Chen, G. Xu, J. Oh, S.-H. Kang, S. Chen, C. Yang, J. Brus, J. Hou, F. Gao, Y. Li, Y. Li, *Nat. Energy* **2021**, *6*, 1045.
[40] M. Günther, N. Kazerouni, D. Blätte, J. D. Perea, B. C. Thompson, T. Ameri, *Nat. Rev. Mater.* **2023**, *8*, 456.
[41] J. Gao, W. Gao, X. Ma, Z. Hu, C. Xu, X. Wang, Q. An, C. Yang, X. Zhang, F. Zhang, *Energy Environ. Sci.* **2020**, *13*, 958.
[42] Y. Gao, X. Yang, W. Wang, R. Sun, J. Cui, Y. Fu, K. Li, M. Zhang, C. Liu, H. Zhu, X. Lu, J. Min, *Adv. Mater.* **2023**, *35*, 2300531.
[43] S. You, Y. Zhang, B. Huang, S. Y. Jeong, X. Shuai, S. Huang, H. Y. Woo, F. Wu, L. Chen, *Adv. Funct. Mater.* **2025**, *35*, 2414803.
[44] X. Ding, X. Wu, S. Li, T. Chen, J. Yu, H. Liu, M. Wang, X.-K. Ye, N. Zhang, X. Lu, C.-Z. Li, H. Zhu, M. Shi, H. Li, H. Chen, *Energy Environ. Sci.* **2025**, *18*, 948.
[45] C. Wang, X. Ma, D. Deng, H. Zhang, R. Sun, J. Zhang, L. Zhang, M. Wu, J. Min, Z.-G. Zhang, Z. Wei, *Nat. Commun.* **2024**, *15*, 8494.
[46] Y. Miao, Y. Sun, W. Zou, X. Zhang, Y. Kan, W. Zhang, X. Jiang, X. Wang, R. Yang, X. Hao, L. Geng, H. Xu, K. Gao, *Adv. Mater.* **2024**, *36*, 2406623.
[47] Y. Cho, Z. Sun, G. Li, D. Zhang, S. Yang, T. J. Marks, C. Yang, A. Facchetti, *J. Am. Chem. Soc.* **2025**, *147*, 758.
[48] L. Ma, H. Yao, J. Wang, Y. Xu, M. Gao, Y. Zu, Y. Cui, S. Zhang, L. Ye, J. Hou, *Angew. Chem., Int. Ed.* **2021**, *60*, 15988.
[49] P. Ding, Z. Chen, D. Yang, X. Yu, J. Shi, Y. Chen, J. Zhu, J. Wu, X. Cao, L. Xie, F. Chen, Z. Ge, *Adv. Mater.* **2025**, *37*, 2414080.
[50] W. Song, Q. Ye, S. Yang, L. Xie, Y. Meng, Z. Chen, Q. Gu, D. Yang, J. Shi, Z. Ge, *Angew. Chem.* **2023**, *135*, 202310034.
[51] J.-W. Lee, T. H.-Q. Nguyen, W. J. Kang, S. Seo, S. Lee, S. Lee, J. Choi, J. Park, J.-Y. Lee, T.-S. Kim, B. J. Kim, *Energy Environ. Sci.* **2025**, *18*, 3325.
[52] H. Gao, B. Fan, L. Yu, Y. Wang, R. Li, W. Jiang, T. Chen, J. Zeng, F. R. Lin, B. Kan, H. Li, L. Wang, A. K.-Y. Jen, *ACS Energy Lett.* **2024**, *9*, 5541.
[53] X. Gu, X. Zhang, H. Huang, *Angew. Chem., Int. Ed.* **2023**, *62*, 202308496.
[54] Z. Zhang, S. Yuan, T. Chen, J. Wang, Y.-Q.-Q. Yi, B. Zhao, M. Li, Z. Yao, C. Li, X. Wan, G. Long, B. Kan, Y. Chen, *Energy Environ. Sci.* **2024**, *17*, 5719.
[55] Y. Li, F. Qi, B. Fan, K. Liu, J. Yu, Y. Fu, X. Liu, Z. Wang, S. Zhang, G. Lu, X. Lu, Q. Fan, P. C. Y. Chow, W. Ma, F. R. Lin, A. K.-Y. Jen, *Adv. Mater.* **2024**, *36*, 2313393.
[56] J. Song, C. Zhang, C. Li, J. Qiao, J. Yu, J. Gao, X. Wang, X. Hao, Z. Tang, G. Lu, R. Yang, H. Yan, Y. Sun, *Angew. Chem., Int. Ed.* **2024**, *63*, 202404297.
[57] L. Zhan, S. Li, Y. Li, R. Sun, J. Min, Z. Bi, W. Ma, Z. Chen, G. Zhou, H. Zhu, M. Shi, L. Zuo, H. Chen, *Joule* **2022**, *6*, 662.
[58] S. Xu, Y. Zhang, Y. Sun, P. Cheng, Z. Yao, N. Li, L. Ye, L. Zuo, K. Gao, *Nano-Micro Lett.* **2024**, *17*, 37.
[59] Z. Peng, Y. Zhang, X. Sun, W. Zhao, F. Bian, Y. Geng, L. Ye, C. Yang, *Adv. Funct. Mater.* **2023**, *33*, 2213248.
[60] J. Zhao, X. Yang, Y. Shao, R. Sun, J. Min, *Sci. China Mater.* **2024**, *68*, 1391.
[61] R. Po, G. Bianchi, C. Carbonera, A. Pellegrino, *Macromolecules* **2015**, *48*, 453.
[62] J. Guo, B. Qiu, D. Yang, C. Zhu, L. Zhou, C. Su, U.-S. Jeng, X. Xia, X. Lu, L. Meng, Z. Zhang, Y. Li, *Adv. Funct. Mater.* **2022**, *32*, 2110159.